Analysis of Crab X-Ray Polarization Using Deeper Imaging X-Ray Polarimetry Explorer Observations

Josephine Wong[1] , Tsunefumi Mizuno[2] , Niccoló Bucciantini[3,4,5] , Roger W. Romani[1] , Yi-Jung Yang[6,7] , Kuan Liu[8] , Wei Deng[8] , Kazuho Goya[9] , Fei Xie[8,10] , Maura Pilia[11] , Philip Kaaret[12] , Martin C. Weisskopf[12] , Stefano Silvestri[13] , C.-Y. Ng[14] , Chien-Ting Chen[15] , Iván Agudo[16] , Lucio A. Antonelli[17,18] , Matteo Bachetti[11] , Luca Baldini[19,20] , Wayne H. Baumgartner[12] , Ronaldo Bellazzini[19] , Stefano Bianchi[21] , Stephen D. Bongiorno[12] , Raffaella Bonino[22,23] , Alessandro Brez[19] , Fiamma Capitanio[10] , Simone Castellano[19] , Elisabetta Cavazzuti[24] , Stefano Ciprini[18,25] , Enrico Costa[10] , Alessandra De Rosa[10] , Ettore Del Monte[10] , Laura Di Gesu[24] , Niccoló Di Lalla[1] , Alessandro Di Marco[10] , Immacolata Donnarumma[24] , Victor Doroshenko[26] , Michal Dovčiak[27] , Steven R. Ehlert[12] , Teruaki Enoto[28] , Yuri Evangelista[10] , Sergio Fabiani[10] , Riccardo Ferrazzoli[10] , Javier A. Garcia[29] , Shuichi Gunji[30] , Jeremy Heyl[31] , Wataru Iwakiri[32] , Svetlana G. Jorstad[33,34] , Vladimir Karas[27] , Fabian Kislat[35] , Takao Kitaguchi[28] , Jeffery J. Kolodziejczak[12] , Henric Krawczynski[36] , Fabio La Monaca[10,37,38] , Luca Latronico[22] , Ioannis Liodakis[12] , Simone Maldera[22] , Alberto Manfreda[39] , Frédéric Marin[40] , Andrea Marinucci[24] , Alan P. Marscher[33] , Herman L. Marshall[41] , Francesco Massaro[22,23] , Giorgio Matt[21] , Ikuyuki Mitsuishi[42] , Fabio Muleri[10] , Michela Negro[43] , Stephen L. O'Dell[12] , Nicola Omodei[1] , Chiara Oppedisano[22] , Alessandro Papitto[17] , George G. Pavlov[44] , Abel Lawrence Peirson[1] , Matteo Perri[17,18] , Melissa Pesce-Rollins[19] , Pierre-Olivier Petrucci[45] , Andrea Possenti[11] , Juri Poutanen[46] , Simonetta Puccetti[18] , Brian D. Ramsey[12] , John Rankin[10] , Ajay Ratheesh[10] , Oliver J. Roberts[15] , Carmelo Sgró[19] , Patrick Slane[47] , Paolo Soffitta[10] , Gloria Spandre[19] , Douglas A. Swartz[15] , Toru Tamagawa[28] , Fabrizio Tavecchio[48] , Roberto Taverna[49] , Yuzuru Tawara[42] , Allyn F. Tennant[12] , Nicholas E. Thomas[12] , Francesco Tombesi[25,50] , Alessio Trois[11] , Sergey Tsygankov[46] , Roberto Turolla[49,51] , Jacco Vink[52] , Kinwah Wu[51] , and Silvia Zane[51]

[1] Department of Physics and Kavli Institute for Particle Astrophysics and Cosmology, Stanford University, Stanford, CA 94305, USA; joswong@stanford.edu
[2] Hiroshima Astrophysical Science Center, Hiroshima University, 1-3-1 Kagamiyama, Higashi-Hiroshima, Hiroshima 739-8526, Japan
[3] INAF Osservatorio Astrofisico di Arcetri, Largo Enrico Fermi 5, 50125 Firenze, Italy
[4] Dipartimento di Fisica e Astronomia, Università degli Studi di Firenze, Via Sansone 1, 50019 Sesto Fiorentino (FI), Italy
[5] Istituto Nazionale di Fisica Nucleare, Sezione di Firenze, Via Sansone 1, 50019 Sesto Fiorentino (FI), Italy
[6] Graduate Institute of Astronomy, National Central University, 300 Zhongda Road, Zhongli, Taoyuan 32001, Taiwan
[7] Laboratory for Space Research, The University of Hong Kong, Cyberport 4, Hong Kong
[8] Guangxi Key Laboratory for Relativistic Astrophysics, School of Physical Science and Technology, Guangxi University, Nanning 530004, People's Republic of China
[9] Hiroshima University, School of Science, 1-3-1 Kagamiyama, Higashi-Hiroshima 739-8526, Japan
[10] INAF Istituto di Astrofisica e Planetologia Spaziali, Via del Fosso del Cavaliere 100, 00133 Roma, Italy
[11] INAF Osservatorio Astronomico di Cagliari, Via della Scienza 5, 09047 Selargius (CA), Italy
[12] NASA Marshall Space Flight Center, Huntsville, AL 35812, USA
[13] Istituto Nazionale di Fisica Nucleare, 56127 Sezione di Pisa, Italy
[14] Department of Physics, The University of Hong Kong, Pokfulam, Hong Kong
[15] Science and Technology Institute, Universities Space Research Association, Huntsville, AL 35805, USA
[16] Instituto de Astrofísica de Andalucía-CSIC, Glorieta de la Astronomía s/n, 18008 Granada, Spain
[17] INAF Osservatorio Astronomico di Roma, Via Frascati 33, 00078 Monte Porzio Catone (RM), Italy
[18] Space Science Data Center, Agenzia Spaziale Italiana, Via del Politecnico snc, 00133 Roma, Italy
[19] Istituto Nazionale di Fisica Nucleare, Sezione di Pisa, Largo B. Pontecorvo 3, 56127 Pisa, Italy
[20] Dipartimento di Fisica, Università di Pisa, Largo B. Pontecorvo 3, 56127 Pisa, Italy
[21] Dipartimento di Matematica e Fisica, Università degli Studi Roma Tre, Via della Vasca Navale 84, 00146 Roma, Italy
[22] Istituto Nazionale di Fisica Nucleare, Sezione di Torino, Via Pietro Giuria 1, 10125 Torino, Italy
[23] Dipartimento di Fisica, Università degli Studi di Torino, Via Pietro Giuria 1, 10125 Torino, Italy
[24] ASI—Agenzia Spaziale Italiana, Via del Politecnico snc, 00133 Roma, Italy
[25] Istituto Nazionale di Fisica Nucleare, Sezione di Roma "Tor Vergata," Via della Ricerca Scientifica 1, 00133 Roma, Italy
[26] Institut für Astronomie und Astrophysik, Universität Tübingen, Sand 1, 72076 Tübingen, Germany
[27] Astronomical Institute of the Czech Academy of Sciences, Boční II 1401/1, 14100 Praha 4, Czech Republic
[28] RIKEN Cluster for Pioneering Research, 2-1 Hirosawa, Wako, Saitama 351-0198, Japan
[29] NASA Goddard Space Flight Center, Greenbelt, MD 20771, USA
[30] Yamagata University,1-4-12 Kojirakawa-machi, Yamagata-shi 990-8560, Japan
[31] University of British Columbia, Vancouver, BC V6T 1Z4, Canada
[32] International Center for Hadron Astrophysics, Chiba University, Chiba 263-8522, Japan
[33] Institute for Astrophysical Research, Boston University, 725 Commonwealth Avenue, Boston, MA 02215, USA
[34] Department of Astrophysics, St. Petersburg State University, Universitetsky pr. 28, Petrodvoretz, 198504 St. Petersburg, Russia
[35] Department of Physics and Astronomy and Space Science Center, University of New Hampshire, Durham, NH 03824, USA
[36] Physics Department and McDonnell Center for the Space Sciences, Washington University in St. Louis, St. Louis, MO 63130, USA
[37] Dipartimento di Fisica, Università degli Studi di Roma "Tor Vergata," Via della Ricerca Scientifica 1, I-00133 Roma, Italy
[38] Dipartimento di Fisica, Università degli Studi di Roma "La Sapienza," Piazzale Aldo Moro 5, I-00185 Roma, Italy
[39] Istituto Nazionale di Fisica Nucleare, Sezione di Napoli, Strada Comunale Cinthia, 80126 Napoli, Italy
[40] Université de Strasbourg, CNRS, Observatoire Astronomique de Strasbourg, UMR 7550, 67000 Strasbourg, France
[41] MIT Kavli Institute for Astrophysics and Space Research, Massachusetts Institute of Technology, 77 Massachusetts Avenue, Cambridge, MA 02139, USA
[42] Graduate School of Science, Division of Particle and Astrophysical Science, Nagoya University, Furo-cho, Chikusa-ku, Nagoya, Aichi 464-8602, Japan
[43] Department of Physics and Astronomy, Louisiana State University, Baton Rouge, LA 70803, USA

[44] Department of Astronomy and Astrophysics, Pennsylvania State University, University Park, PA 16802, USA
[45] Université Grenoble Alpes, CNRS, IPAG, 38000 Grenoble, France
[46] Department of Physics and Astronomy, University of Turku, FI-20014, Finland
[47] Center for Astrophysics | Harvard & Smithsonian, 60 Garden Street, Cambridge, MA 02138, USA
[48] INAF Osservatorio Astronomico di Brera, Via E. Bianchi 46, 23807 Merate (LC), Italy
[49] Dipartimento di Fisica e Astronomia, Università degli Studi di Padova, Via Marzolo 8, 35131 Padova, Italy
[50] Dipartimento di Fisica, Università degli Studi di Roma "Tor Vergata," Via della Ricerca Scientifica 1, 00133 Roma, Italy
[51] Mullard Space Science Laboratory, University College London, Holmbury St Mary, Dorking, Surrey RH5 6NT, UK
[52] Anton Pannekoek Institute for Astronomy & GRAPPA, University of Amsterdam, Science Park 904, 1098 XH Amsterdam, The Netherlands

Abstract

We present Crab X-ray polarization measurements using Imaging X-Ray Polarimetry Explorer (IXPE) data with a total exposure of 300 ks, three times more than the initial 2022 discovery paper. Polarization is detected in three times more pulsar phase bins, revealing an S-shaped $+40°$ polarization angle sweep in the main pulse and $>1\sigma$ departures from the OPTIMA optical polarization in both pulses, suggesting different radiation mechanisms or sites for the polarized emission at the two wavebands. Our polarization map of the inner nebula reveals a toroidal magnetic field, as seen in prior IXPE analyses. Along the southern jet, the magnetic field orientation relative to the jet axis changes from perpendicular to parallel and the polarization degree decreases by $\sim 6\%$. These observations may be explained by kink instabilities along the jet or a collision with a dense, jet-deflecting medium at the tip. Using spectropolarimetric analysis, we find asymmetric polarization in the four quadrants of the inner nebula, as expected for a toroidal field geometry, and a spatial correlation between polarization degree and photon index.

Unified Astronomy Thesaurus concepts: Pulsar wind nebulae (2215); Pulsars (1306); Polarimetry (1278); X-ray astronomy (1810)

1. Introduction

Pulsar wind nebulae (PWNe) are highly energetic astrophysical sources that consist of a central spinning neutron star (pulsar) whose powerful magnetic field ($B \sim 10^{12}$ G) generates a wind of relativistic ($\gamma \gtrsim 10^5$) electrons and positrons that escape along open field lines, impinging on and carrying energy into the surrounding supernova (SN) ejecta or interstellar medium (ISM; Kirk et al. 2009). They can be detected across the entire electromagnetic spectrum with a nonthermal spectral energy distribution that displays a synchrotron bump that extends from the radio to hard X-rays (up to MeV energies) and an inverse Compton bump that can reach up to TeV (Slane 2017) or even PeV (Liu & Wang 2021) energies. Spatially resolved observations reveal time-varying structures such as wisps, knots, filaments, and polar jets that point to an ongoing resupply of energy whose source we now know to be the pulsar.

The pulsar itself is seen as a bright point source at the center of the PWN and its radiative signature is the pulsed light curve. The origin of this radiation is believed to be located close to the boundary of the light cylinder radius, the distance at which the corotation velocity is equal to the speed of light. Interactions between charged particles (electrons and positrons) and magnetic fields at the light cylinder generate pulsed, polarized emission. The physical mechanism behind the pulsed emission is still an open question—a variety of models exist, each with different predictions for the pulse shape and polarization. Thus, polarization measurements of the pulsar can help constrain emission models.

The Crab is one of the best-studied objects in astrophysics. It is located ~ 2 kpc from Earth (Trimble 1973), and with nebular

luminosity $L \sim 1.3 \times 10^{38}$ erg s^{-1} (Hester 2008), it is bright enough to allow study of its morphology in great spatial detail with high statistical precision. At its center, the $P = 33.6$ ms PSR J0534+2200 is surrounded by a synchrotron nebula G184.6-5.8 that radiates strongly from radio to gamma-ray energies (Ansoldi et al. 2016). The inner nebula has polar jets and an equatorial torus wrapped around the termination shock that are prominent in X-rays. It is encased in a bubble-like structure of optical filaments formed by SN ejecta carving out cavities in the ambient ISM, with "finger-like" protrusions extending inward from the filaments toward the lower-density synchrotron nebula. Diffuse radio emission exists throughout the nebula (Hester 2008).

Polarization has been detected in both G184.6-5.8 and PSR J0534+2200. The first polarization measurements were made in 1954 at optical energies by two independent researchers (Dombrovsky 1954; Vashakidze 1954); high polarization levels confirmed the synchrotron origin of the nebular radiation, as suggested by Shklovsky (1953). This was the first identification of synchrotron radiation in any astrophysical source. Radio polarization measurements soon followed (Mayer et al. 1957) and later, with the advent of photon-scattering polarimeters, soft X-rays (Novick et al. 1972; Weisskopf et al. 1978), hard X-rays (Chauvin et al. 2017), and gamma rays (Dean et al. 2008). In each of these cases, the electric vector polarization angle (PA) integrated across the nebula was approximately along the torus symmetry axis ($\sim 125°$, east of north), implying an azimuthal magnetic field (Bühler & Blandford 2014).

Technological advances also later enabled temporal optical polarization studies, which allowed for phase-resolved analysis and separation of the pulsar and nebula components through isolation of the off-phase emission. In one of the most detailed optical studies of the Crab pulsar, Słowikowska et al. (2009) found that the PA has a rapid monotomic sweep of about $+130°$ through the main pulse (MP) and $+100°$

through the interpulse (IP) and that the polarization degree (PD) seems to increase to a maximum before each pulse, then rapidly fall to a minimum close to the peak intensity. High-angular-resolution nebula polarization studies have also been conducted at optical energies (Moran et al. 2013) and reveal high polarization levels in the inner knot and wisps (∼60% and ∼40%, respectively), with directions oriented close to the pulsar spin axis. Similar studies at higher energies (e.g., X-rays) can provide critical information about the radiation of electrons and positrons closer to their injection site.

The Imaging X-Ray Polarimetry Explorer (IXPE; Weisskopf et al. 2022), the first space observatory dedicated to measuring X-ray polarization, has enabled these observations in the soft X-rays. With a nominal 2–8 keV energy range, $<100\,\mu s$ resolution, and $<30''$ half-power diameter (HPD), IXPE has detected polarization in several PWNe and even a few phase bins near the pulse peak for the brightest pulsars (Xie et al. 2022, 2024; Romani 2023), including the Crab (Bucciantini et al. 2023b).

In 2022, IXPE observed the Crab for 90 ks. Bucciantini et al. (2023b) detected PD = 15.4% and PA = 105° in the MP after "off-pulse" (OP) subtraction (the interval between the end of the IP and the start of the MP, when the pulsar flux is at a minimum). They also measured PD = 24.1% and PA = 133° in the OP. The phase-integrated polarization map revealed a toroidal magnetic field wrapped around the pulsar and asymmetric PD that does not align with the intensity map. Using an improved method to separate the pulsar and the nebula polarized fluxes, Wong et al. (2023) measured polarization in two MP phase bins (PD = 9%, PA = 97° followed by PD = 15%, PA = 103°) and one IP phase bin (PD = 16%, PA = 141°). There was suggestion of a PA sweep through the MP, but more measurements were necessary to establish a clear pattern. They also extracted a polarization map for the pulsar-cleaned nebula, finding a toroidal magnetic field and PD asymmetries similar to those found in Bucciantini et al. (2023b). Mizuno et al. (2023) analyzed the nebula's magnetic field structure, including a comparison with a polarization model, and deferred spectropolarimetric analysis for future studies due to uncertainties in the spectral response at the time.

In 2023, IXPE observed the Crab for an additional 210 ks. In this paper, we analyze the full 300 ks IXPE data set of the Crab, which yields a ∼1.8 times boost in signal-to-noise ratio and reduced systematic uncertainty relative to the initial discovery paper. Section 2 describes the IXPE observations and the Chandra image used in the data analysis. Section 3 presents the XSPEC spectral analysis of the nebula and its subregions. Section 4 summarizes the reduction process for polarization, utilizing the simultaneous fitting technique of Wong et al. (2023), and presents the nebular polarization map and the phase-varying pulsar polarization. Section 5 discusses possible physical interpretations of the spectral and polarization measurements.

2. Observations

IXPE observed the Crab at three different epochs with a total ontime of about 300 ks: (1) 2022 February 21–2022 March 8; (2) 2023 February 22−2023 April 3; and (3) 2023 October 9 −10. Among all observations, the average livetime:ontime ratio was 0.923. Associated with this campaign, the Chandra X-ray Observatory (CXO) observed the Crab for an effective

1.33 ks exposure on 2022 March 15, one week after the first IXPE exposure.

2.1. IXPE

The first IXPE Crab observation (ObsID 01001099) was conducted in two segments: the first segment from 2022 February 21 to 22 with a spacecraft roll angle of 158°.0 (east of north) and the second segment from 2022 March 7 to 8 with a roll angle of 158°.3. The ontimes for each segment were ∼43 ks and ∼49 ks, respectively. Because the offset between the optical axis and the spacecraft axes had not yet been measured and could not be taken into account during the target pointing, the optical axis was displaced from the target by ∼ 2.′74. We used the CIAO tool ixpecalcarf to generate effective area and modulation response functions accounting for this offset, using the latest on-axis response files in the HEASARC CALDB database (XRT version 20231201, GPD version 20240125).

The second IXPE Crab observation (ObsID 02001099) was conducted in two segments: the first segment from 2023 February 22 to 23 with a roll angle of 158°.0 and the second segment from 2023 April 1 to 3 with a roll angle of 158°.9. Each segment's ontime was ∼74 ks.

The third IXPE Crab observation (ObsID 02006001) was conducted in one segment from 2023 October 9 to 10 with a roll angle of 339°.0 and ∼ 60 ks ontime.

For the second and third IXPE observations, we made vignetting-corrected response functions using ixpecalcarf. This was necessary to obtain a good agreement in the fitted spectral flux (see Section 3) between the observations with 2%–3% residual differences.

We obtained the Level 2 data files for these observations from the HEASARC archive.[53] All data files were processed with the following steps before data analysis. (1) Particle and instrumental background events were removed according to the Di Marco et al. (2023) algorithm and by filtering for the good time intervals (GTIs). The Di Marco background rejection algorithm removed less than 2% of the total events. The GTI filter, which excludes observational periods with poor aspect (Baldini et al. 2022), removed less than 1% of events from each detector unit (DU). (2) Barycentric correction was performed using the barycorr tool in HEASoft V6.30.1. The JPL-DE430 solar ephemeris was utilized, with the position of the source set at R.A. = $5^h34^m31^s.86$ and decl. = $22°00'51''.3$ (J2000). (3) The World Coordinate System was boresighted by comparing the $125'' \times 125''$ Stokes I data map centered on the pulsar in the MP window ($\Delta = 0.963$–0.987) with the simulated Stokes I map and adjusting each observation's R.A. and decl. in $0''.1$ increments to minimize the χ^2-value. See Section 4 for a description of the simulation procedure. By using the MP window, the alignment is keyed to the pulsar position, set at the aforementioned R.A. and decl. This aspect correction, while small (typically ∼1″, always <4″), proved quite important to polarization measurements, improving the agreement of the IXPE data with our flux model by a factor of ∼3.5×. (4) The pulse profile was folded with the ixpeobssim software xpphase tool. Table 1 lists the Jodrell Bank Observatory (JBO) ephemeris used for each observation epoch.

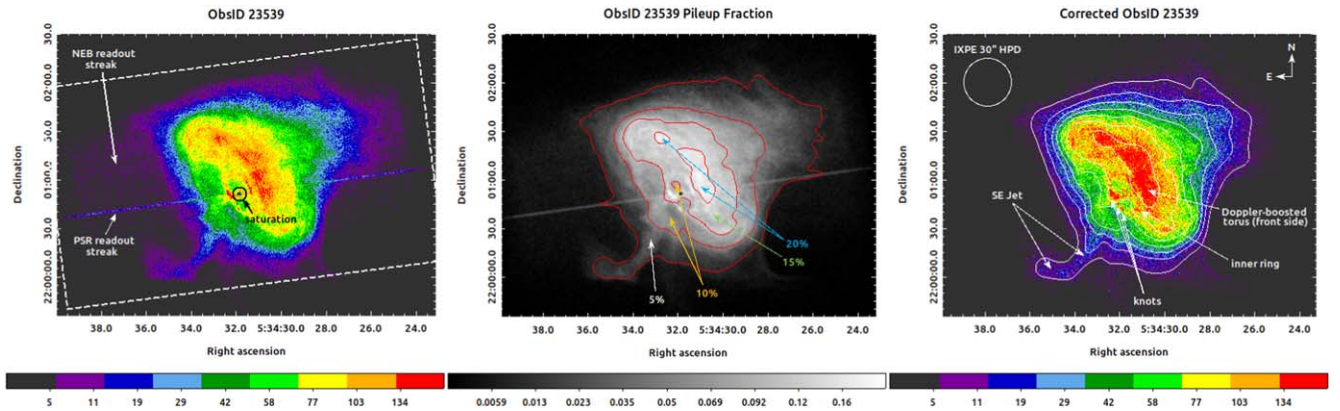**Figure 1.** Chandra ObsID 23539 of the Crab Nebula before (left) and after (right) processing, displaying a $3.'9 \times 2.'9$ region. Images are matched in log scale. CCD readout streaks and photon pileup at the pulsar position and throughout the nebula in the original Level 2 event file were corrected. The center image shows a map with red isocontours of the pileup fraction in the nebula, which reaches up to ~20% in the Doppler-boosted region. See Section 2.2 for a discussion of the processing technique.

Table 1
JBO Ephemerides Used in the Phase Folding of the IXPE Crab Observations

Parameters	Ephemeris 1	Ephemeris 2	Ephemeris 3
JBO Month	2022 March	2023 February	2023 September
PEPOCH (MJD)	59625	59990	60202
ν (Hz)	29.5870753202	29.5754926637	29.5687705364
$\dot{\nu}$ (10^{-10} Hz s^{-1})	−3.67470	−3.67089	−3.66897
$\ddot{\nu}$ (10^{-21} Hz s^{-2})	8.04	5.24	11.6

Note. Ephemeris 1 was applied to ObsID 01001099, Ephemeris 2 to ObsID 02001099, and Ephemeris 3 to ObsID 02006001.

2.2. Chandra

CXO ObsID 23539 was obtained on 2022 March 15, one week after the conclusion of the first IXPE Crab observation. It was taken in 1:16 subframe mode (0.2 s frame time) for 10 ks for a total livetime of 1.33 ks. These data were used to simulate the IXPE observation of the Crab PWN by passing the Level 2 event file through the IXPE instrument response using the `ixpeobssim V31.0.1` tool `xpobssim` and instantiating an `xChandraObservation` object. See Section 4 for more details about the simulation procedure. Our IXPE observations extend out ~2.5 yr from the CXO observation. The bright inner wisps vary on a year timescale, but the expected shifts are too small to affect the intensity on the IXPE point-spread function (PSF) scale. Somewhat larger shifts are associated with the southern jet, but they appear on the decade timescale, so our CXO reference should be adequate.

Several artifacts needed to be removed from the Level 2 event file to produce a good-quality file for use. Wong et al. (2023) noted two artifacts—CCD saturation at the pulsar position and readout streaks due to out-of-time events from the pulsar and the nebula—and reported correction methods. Here, we describe an improved technique for removing the nebula readout streak that reduces artificial jumps due to sampling in discrete regions. A $495'' \times 345''$ rectangle tilted along the readout direction encompassing the nebula readout streak was divided into a grid of $15'' \times 15''$ pixels. For each row, we estimated the excess counts and subtracted it from each pixel in that row. By correcting in smaller regions and adjusting the number of excess counts for each row, we produce a smoother readout-corrected image with fewer trail artifacts.

We also found that pileup, which occurs when two or more events land on a CCD pixel within the same readout frame, was present in our CXO observation. The CIAO tool `pileup_map` reported pileup fractions as high as ~20% in the bright Doppler-boosted northwest region of the nebula. Pileup effects underestimate the local count rate and distort the spectrum. To correct for this, we renormalized the number of counts by $1/(1 - p_f)^{1.5}$, where p_f is the reported pileup fraction for a given pixel. The 1.5 exponent heuristically addresses the effect of spectral distortions on the count rate. Note that this renormalization scheme only corrects the count rate and does not fix the spectrum. To do so, we would need to run a forward model of the pileup distortion with a template of the true spectrum of the nebula, which was not available. To minimize the effect of this spectral distortion on the polarization measurements, we have used a single 2–8 keV energy band in our analysis. See Figure 1 for images before and after correcting for these artifacts, as well as a distribution map of the pileup fraction across the nebula.

3. XSPEC Spectral Analysis

We performed XSPEC spectropolarimetric analysis to investigate the positional dependence of spectral and polarization properties in the nebula. We defined a small ellipse, hereafter called "Region 1," which contains the central X-ray torus, with major and minor axes of $41.''3$ and $18.''8$ and a position angle of $126.°3$ (Ng & Romani 2004). We defined two outer regions, Region 2 and Region 3, with the same area as Region 1 and with respective inner and outer radii of $26.''6$, $58.''4$ and $32.''6$, $71.''5$. Both regions were further divided along the major and minor axes into four subregions, referred to as "Region 2N," "Region 3N," etc. See Figure 2 for a diagram of the selected regions.

We extracted the Stokes I, Q, and U spectra of each region using the standard software `ixpeobssim V31.0.1`. For Region 1, we used only data in the OP period ($\Delta = 1.563$–1.863), to minimize pulsar contamination. For the other regions, the spectral and polarimetric parameters change by less than 5% if we use all data, so we do not apply a phase cut to simplify the analysis. For background subtraction, we extracted a spectrum from an annulus centered on the pulsar position with an inner and outer radius of $2.'5$ and $3.'0$, respectively. We found that the background has negligible

Table 2
Summary of the Spectral Fits of the Crab PWN

Region	Absorption $(10^{22}\,\mathrm{cm}^{-2})$	Index	Absorbed Flux (2–8 keV) $(10^{-9}\,\mathrm{erg\,s}^{-1}\,\mathrm{cm}^{-2})$	PD	PA (deg)	χ^2/DoF
Region 1	0.26 ± 0.02	2.160 ± 0.007	4.50	0.239 ± 0.003	137.8 ± 0.3	265.7/202
Region 2N	0.30 (fix)	2.234 ± 0.003	1.24	0.214 ± 0.003	152.1 ± 0.4	322.6/203
Region 2E	0.30 (fix)	2.233 ± 0.004	0.65	0.132 ± 0.004	134.6 ± 0.8	241.1/203
Region 2S	0.30 (fix)	2.303 ± 0.005	0.34	0.371 ± 0.005	150.8 ± 0.4	236.3/199
Region 2W	0.30 (fix)	2.164 ± 0.003	0.91	0.116 ± 0.003	135.7 ± 0.8	254.0/203
Region 3N	0.30 (fix)	2.323 ± 0.003	0.77	0.257 ± 0.004	157.0 ± 0.4	282.6/203
Region 3E	0.30 (fix)	2.350 ± 0.005	0.31	0.098 ± 0.006	128.0 ± 1.6	207.5/198
Region 3S	0.30 (fix)	2.375 ± 0.007	0.16	0.363 ± 0.008	152.0 ± 0.6	214.4/192
Region 3W	0.30 (fix)	2.199 ± 0.004	0.57	0.088 ± 0.004	125.0 ± 1.4	264.1/203

effects for all regions and we do not subtract it in the spectral analysis for simplicity. As first discussed by Bucciantini et al. (2023a), we also needed to address the effect of "leakage," which is the spatial spreading of polarized flux, preferentially in the direction of the polarization, due to imperfect reconstruction of the photon position in the IXPE detector. Dinsmore & Romani (2024b) present a correction technique using detailed 2D sky-calibrated IXPE PSFs with a code library publicly available in the Github repository `leakagelib`.[54] Using the code and the polarization parameters obtained through simultaneous fitting (see Section 4), we generated 5″ Stokes I, Q, and U leakage maps binned into four energy bands (2–2.8, 2.8–4, 4–5.6, and 5.6–8 keV). For each region, we extracted the Stokes I, Q, and U leakage spectra, normalized by the Stokes I spectrum, and fit them with a power-law model. Then we calculated the model leakage spectrum in the standard energy binning (0.04 keV) and subtracted it from the total spectrum.

Using our leakage-corrected Stokes I, Q, and U spectra, we performed spectropolarimetric fits using the `xspec` command in `HEASoft V6.32.1` with an absorbed power-law model and energy-independent polarization (`tbabs×powerlaw×polconst` in `xspec`). To mitigate the low photon statistics, we fixed the absorption density to the canonical value of $0.3 \times 10^{22}\,\mathrm{cm}^{-2}$ (Mori et al. 2004) for regions other than Region 1. We fitted the Region 1 absorption density to obtain better fit statistics, but the fitted value remained close to (within 2σ of) the canonical value. The fit results are summarized in Table 2 (with 1σ statistical errors) and Figures 2 and 3.

We were able to obtain agreement of the total flux within 2%–3% between observations. Our photon indices are systematically larger by a few percent than those reported in the literature. For example, we find a photon index of 2.160 ± 0.007 for the central region, but Mori et al. (2004) report values around ~2.0 for the inner nebula. This difference is likely due to contributions from the softer, outer regions of the nebula (Weisskopf et al. 2000) and possibly also instrument calibration. The effects on the polarization parameters and the relative values of the spectral parameters should be much smaller.

4. Simultaneous Fit Polarization

We used the simultaneous fitting technique described in Wong et al. (2023) to extract the nebula and the pulsar polarization parameters. The technique requires a model for the pulsar and the nebula flux as a function of phase, energy, and
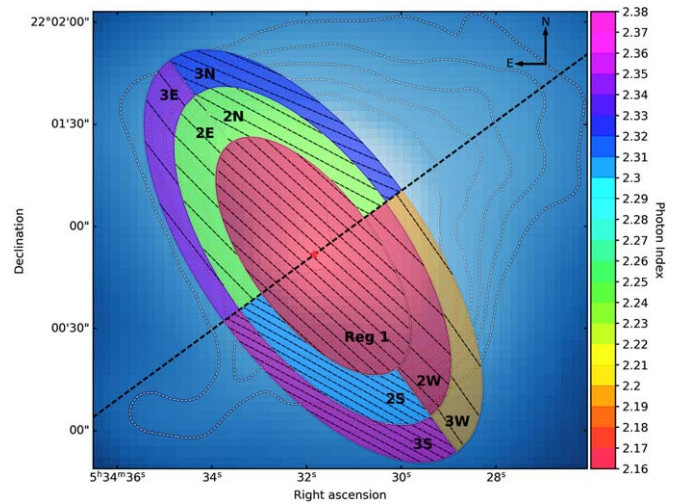
Figure 2. Spectropolarimetric analysis of selected regions of the Crab Nebula labeled according to Table 2. The shading represents the photon index. The crosshatched lines represent the magnetic field direction with line density = 13″/PD. The background blue heat map overlaid with the white contours (the same as from Figure 1, right panel) represents the IXPE count distribution. The dashed black line is the torus symmetry axis. The red star indicates the location of the pulsar.

spatial position. The Crab pulsar model was created by running an `ixpeobssim` simulation of a periodic point source with phase-varying spectral parameters obtained from CXO HRC-LETGS data by Weisskopf et al. (2011). The Crab Nebula model was made by instantiating an `xChandraObservation` object with the artifact-cleaned CXO ObsID 23539 in `ixpeobssim`. For both models, the different efficiencies of the CXO and IXPE detectors were accounted for by passing the CXO measurements through the ratio of the IXPE:CXO effective areas and applying the IXPE PSF. A 750 ks simulation, more than 10 times longer than any one segment exposure, was generated for each segment using its specific telescope roll and instrument response function and normalized by its specific ontime duration. A small scaling factor was applied to match the simulated and the observed IXPE light curves. The pulsar scaling factor was ~0.75 and the nebula scaling was ~0.90. A small normalization constant, fixed at 1 for DU1 and within 3.5% for the other DUs, was applied for each DU to account for calibration differences.

Note that the Weisskopf et al. (2011) Crab pulsar spectrum was derived using 0.3–3.8 keV CXO data within a radius of 1″63. The spectral analysis done by Massaro et al. (2000) with BeppoSAX MECS used 1.6–10 keV data, closer to the IXPE
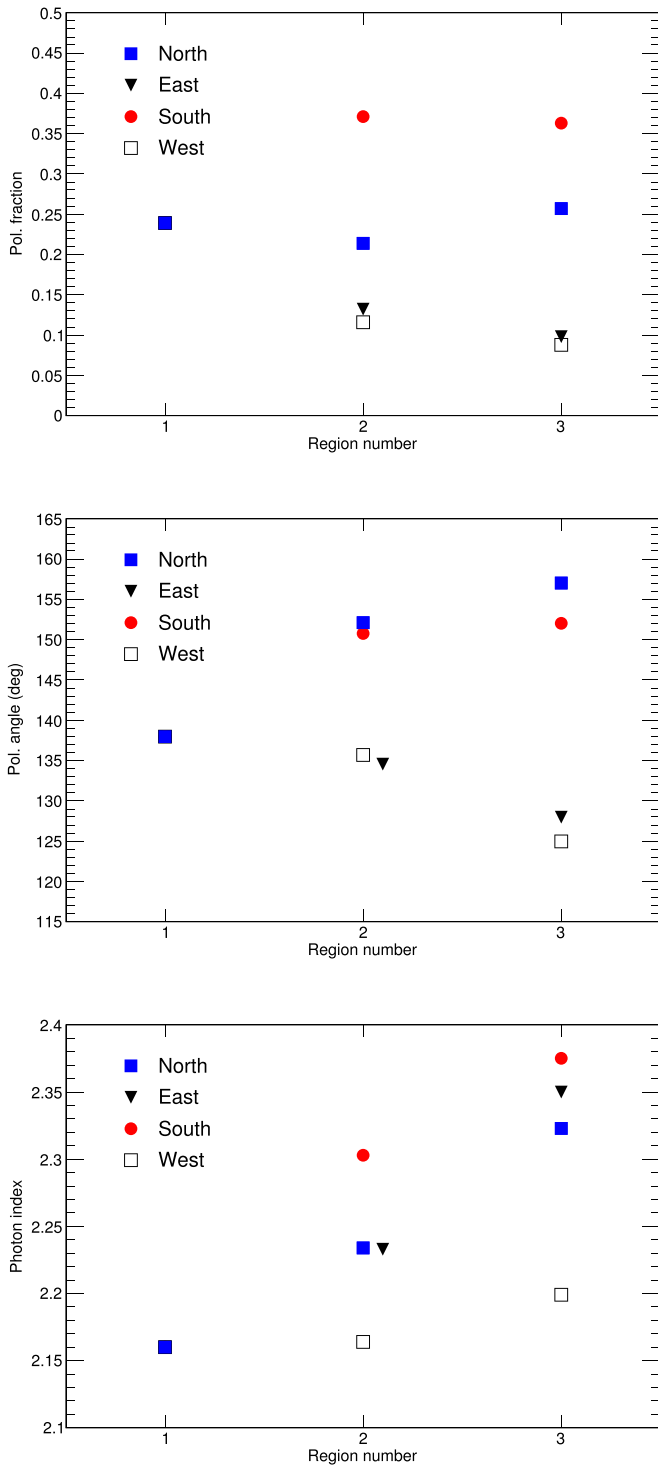
Figure 3. Spectropolarimetric fits for different regions of the Crab Nebula. Error bars are small, comparable to the marker size, and not presented. Region 2E has been shifted horizontally in the middle and bottom panels for clarity. The PD and PA diverge between the north/south and east/west regions, as expected from a toroidal magnetic field. The photon index increases with radius, as might be anticipated due to synchrotron burnoff. It is also asymmetric relative to the torus symmetry axis, with the hardest emission in the west with the lowest PD, and the softest emission in the south with the highest PD.

nominal energy range, but with an extraction radius of $4'$, which has considerably more nebula contribution. They measured phase-varying photon indices about $+0.2$ larger than those found by Weisskopf et al. (2011). To test the sensitivity

of our method to the spectral model, we ran the same analysis using a softer pulsar spectrum with photon indices boosted by $+0.2$ and found that the Stokes q and u parameters differed by at most $\sim 1.5\sigma_{\text{error}}$ of the original fit for the pulsar and $0.3\sigma_{\text{error}}$ for the nebula. Weisskopf et al. (2011) isolate the pulsar more reliably than Massaro et al. (2000), due to the use of a smaller extraction region, so the larger photon index measured by Massaro et al. (2000) should at least partially be attributed to nebula contamination. Therefore, these values represent upper limits for the uncertainty of our measurements due to the imperfect estimate of the pulsar photon index.

To correct for "leakage" effects, we took an iterative approach to estimating and subtracting the leakage from the data and finding the leakage-corrected polarization parameters: (1) an initial fit for the polarization is performed using uncorrected IXPE data; (2) these parameters are input into `leakagelib` to calculate the Stokes I, Q, and U leakage, which we subtract from the data; (3) we fit for new polarization parameters using the leakage-corrected data set; and (4) this process is repeated until the average fractional change of the parameters is less than 10^{-5}, a standard value used in (i.e., Python) software packages for relative comparisons. We found that about three iterations were required to reach convergence and that the Stokes q and u parameters changed more substantially (within about ± 0.03) for the nebula; for the pulsar, most (95%) of the bins changed within ± 0.01.

As described in Wong et al. (2023), simultaneous fitting is a binned analysis method. For our analysis, we used 20 variable-width phase bins, tailored to be narrower in the pulses, to probe the rapid sweep of the pulsar polarization at these phases, and a 13×13 $15''$ grid of spatial pixels. See Table 3 for the exact phase bin selection in the MP and IP. Since the leakage correction algorithm requires fine (max $5''$) spatial bins to resolve the PSF structure, we calculated the leakage with $5''$ pixels and regrouped them into $15''$ pixels before subtracting it from the binned data.

For energy binning, we used a single 2–8 keV bin, because finer energy binning significantly increases the number of low-count (<10 counts) bins. Our fitting approach solves for the polarization parameters using least-squares regression and thus assumes Gaussian-distributed data. For N events with the ψ-distribution function described in Kislat et al. (2015), Stokes Q and U are essentially Gaussian by $N = 10$. With the aforementioned phase and spatial binning and three equally spaced energy bins within 2–8 keV, 52% of data bins would have fewer than 10 counts, about half from the 6 to 8 keV energy bin. Without energy binning, 14% of the bins exceed 10 counts. To use energy bins while minimizing low-count bins, we could use fewer phase bins or larger pixels, but this would degrade the resolution of the rapid changes in polarization from the pulsar emission and/or oversmooth the PSF structure, which separates the pulsar from the nebula flux. The nebula is indeed softer, with a photon index of ~ 2 (Willingale et al. 2001; Mori et al. 2004) compared to ~ 1.4–1.7 (Weisskopf et al. 2011) for the pulsar, so an energy-dependent analysis could make a slight improvement in separating the pulsed and the nebular signals. However, this would require substantial additional exposure or a full Poisson statistics likelihood analysis (which would be much more computationally expensive than our least-squares solution), and so we have elected to retain the best spatial and temporal resolution in a single energy bin.

Table 3
Significant (>3σ) and Marginally Significant (>1.9σ, Dagger) X-Ray Polarization Measurements of the Crab Pulsar

					PD (%)	PA (deg)
		Phase	q	u		
P1	2[†]	0.893–0.923	0.0108 ± 0.0638	−0.1446 ± 0.0637	14 ± 6	137 ± 13
	4[†]	0.953–0.963	−0.0852 ± 0.0311	−0.0079 ± 0.0311	9 ± 3	93 ± 10
	5	0.963–0.973	−0.0829 ± 0.0228	−0.0336 ± 0.0228	9 ± 2	101 ± 7
	6	0.973–0.983	−0.1036 ± 0.0179	−0.0433 ± 0.0179	11 ± 2	101 ± 5
	7	0.983–0.988	−0.1352 ± 0.0203	−0.0753 ± 0.0203	15 ± 2	105 ± 4
	8	0.988–0.993	−0.0831 ± 0.0186	−0.0987 ± 0.0186	13 ± 2	115 ± 4
	9	0.993–0.998	−0.0741 ± 0.0190	−0.0577 ± 0.0190	9 ± 2	109 ± 6
	10	0.998–1.003	−0.0534 ± 0.0216	−0.0539 ± 0.0216	8 ± 2	113 ± 8
	11[†]	1.003–1.028	−0.0047 ± 0.0190	−0.0455 ± 0.0190	5 ± 2	132 ± 12
P2	15[†]	1.268–1.348	−0.0066 ± 0.0265	−0.0502 ± 0.0265	5 ± 3	131 ± 15
	16	1.348–1.378	−0.0425 ± 0.0179	−0.0364 ± 0.0179	6 ± 2	110 ± 9
	17[*]	1.378–1.398	−0.0225 ± 0.0163	−0.0079 ± 0.0163	2 ± 2	100 ± 20
	18	1.398–1.423	−0.0374 ± 0.0195	−0.0649 ± 0.0195	7 ± 2	120 ± 7
	19[†]	1.423–1.563	−0.0466 ± 0.0624	−0.1168 ± 0.0623	13 ± 6	124 ± 14

Note. One ~1.5σ P2 phase bin (starred) has been included for continuity. Refer to Figures 6 and 7 for visual representations of the phase-resolved pulsar measurements. Note that the marginally significant measurements have significant PD−PA covariance, so the 1D errors reported here are not fully representative. (Stokes q and u are independent, so their 1D errors are reliable.) Phases are numbered starting from 1.

In summary, we have utilized the simultaneous fitting technique to separate the nebula and the pulsar polarization parameters. This technique requires Stokes I models, which we generated by taking the nebula spectral map and the pulsar phase-varying spectrum obtained from CXO observations and passing them through the IXPE instrument response. The model and the data were binned into 20 variable-width phase bins and 13×13 15″ pixels and an energy range of 2–8 keV. Leakage removal was performed in conjunction with the simultaneous fitting in an iterative process using the leaka-gelib code. The fit statistic of our final iteration was $\chi^2_{\rm red} = 1.23$, with $\chi^2 = 124066.0$ and DOF = 100708. The $\chi^2_{\rm red} > 1$ may possibly be due to remaining mismatches between the observation and our flux model. Our model can be further refined with improved calibration of the instrument response functions, correction of pileup spectral effects in the CXO image, energy-dependent PSFs, and joint IXPE/CXO observations to obtain the most current state of the nebula.

4.1. Crab Nebula

The Crab Nebula polarization map is depicted in Figure 4. The black lines indicate the magnetic field direction, perpendicular to the measured electric vector polarization angle (EVPA), with lengths scaled by the PD. A 5σ significance cut and 20,000 count flux cut have been applied. The most polarized regions are located at the north and south edges of the torus, with the highest PD = (44 ± 1)% and PD = (47 ± 1)% in these regions, respectively. Two pixels in the jet have significant polarization: one in the body, where the magnetic field appears perpendicular to the jet, and another at the tip, where it appears parallel, with PD = (22 ± 2)% and
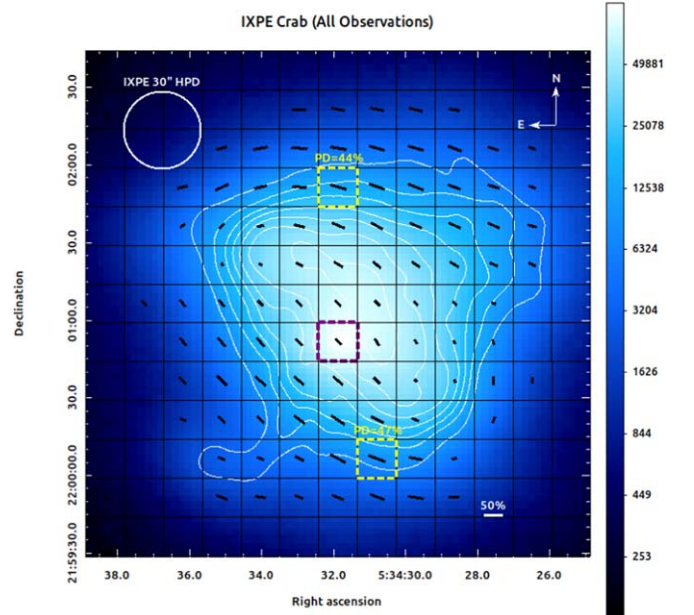

Figure 4. IXPE Crab count map, cropped to the region used for polarimetric analysis (3.′25 × 3.′25), displayed in log scale, combining all three data epochs. The same white contours as in Figure 1 (right panel) demonstrate the effect of IXPE <30″ HPD on the flux distribution. Fine nebular features in the CXO image (like the inner ring) are not visible, although the outer torus and southern jet can be discerned. The black boxes show the 15″ grid used in the simultaneous fitting analysis. The black lines (perpendicular to the IXPE X-ray EVPA) reveal the toroidal magnetic field. Their lengths represent the PD, with PD = 50% shown for reference. Only pixels with >5σ detection and more than 20,000 counts have polarization bars plotted. PSR J0534+2200 is located at the center of the purple dotted box. High-PD regions in the north and south are labeled.
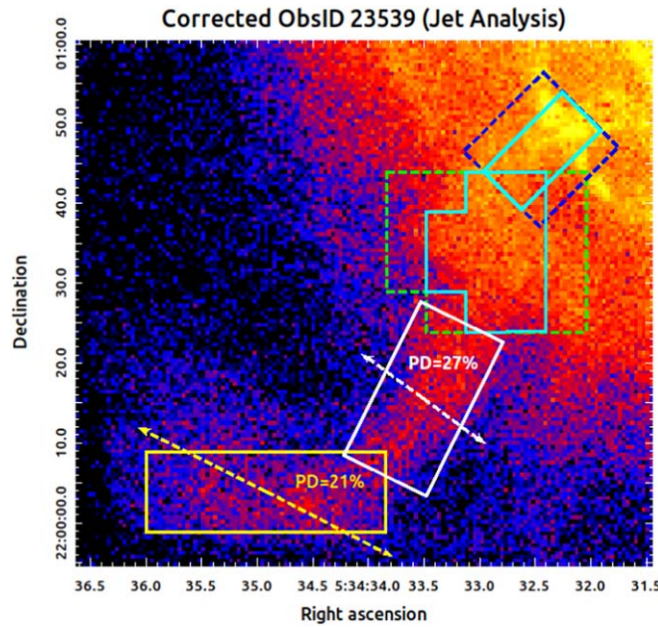
Figure 5. Analysis of the Crab Nebula jet polarization. The jet was divided into the yellow (tip), white (body), and cyan (base) regions. The green and blue dashed boxes represent the flanking regions used for background subtraction. No conclusive measurements in the base were made. In the body and tip, the PD is labeled and the magnetic field direction (perpendicular to the PA) is indicated by the dashed arrows. CXO ObsID 23539 is displayed in the background to visualize the locations of the regions along the jet.

PD $=(19 \pm 2)\%$, respectively. To investigate the jet polarization further, we performed simultaneous fitting with 25×25 5″ pixels (and 16 phase bins, to minimize the percentage of low-count bins to $\sim 10\%$) to obtain a higher-resolution map, divided the map into different regions along the jet, and determined the integrated polarization in each region. We verified that the 5″ polarization map is consistent with that of the original binning, with the most polarized regions located in the same high-PD regions labeled in Figure 4 and having similar PD and PA values throughout the nebula.

Figure 5 depicts the result of the jet analysis. We created four regions along the jet: two cyan regions at the base (with the bracketing blue and green regions for background subtraction) and one region each for the body (white) and the tip (yellow). For the tip and body, no background subtraction was necessary, since the torus does not overlap. We simply summed the pixels within each region and found that the body is polarized with PD $= (27 \pm 1)\%$ and PA $= (144 \pm 1)°$ and the tip is polarized with PD $= (21 \pm 2)\%$ and PA $= (153 \pm 3)°$. As shown in Figure 5, these PAs suggest that the magnetic field is oriented perpendicular and parallel relative to the jet axis in the body and the tip, respectively. Only 5″ pixels with $>3\sigma$ polarization measurements were included in the calculation.

Some concern might be made about the potential for contamination from the torus and adjacent jet regions. Indeed, using ixpeobssim to simulate the central nebula region and the two jet regions individually, we estimate that the torus contributes approximately 23% and 7% of the total flux in the body and tip regions, respectively, the body contributes $\sim 13\%$ of the total flux in the tip, and the tip contributes $\sim 5\%$ of the total flux in the body. This means that 28% and 20% of the flux in the body and the tip, respectively, may be attributed to these regions. In fact, the total background fraction, including

contributions from other areas of the nebula, is estimated to be $\sim 60\%$ and $\sim 50\%$ for the body and the tip, respectively. To determine how significantly the background affects our measurements, we ran a simultaneous fitting procedure, where we included the effect of the PSF flux redistribution in the nebula (it is always computed for the pulsar). That is, for each 5″ pixel, we modeled its contribution to each of the other pixels in the flux map. Using this model should eliminate background contributions on greater than 5″ scales. For this fine pixel scale, we needed additionally to regularize the cost function (the objective function that is minimized in the least-squares analysis), with a penalty for large swings between adjacent pixels. We obtained polarization values consistent with our standard analysis, with PD $= 30\%$ and PA $= 145°$ in the body and PD $= 22\%$ and PA $= 159°$ at the tip. This suggests that our polarization measurements are not significantly biased by the background. However, given the high background percentage, the true uncertainty may be larger than the simple statistical error reported here. Higher spatial resolution would be helpful for isolating the jet polarization more confidently.

We also attempted to measure the polarization in the base regions. Since the jet overlaps with the torus in these regions, we selected flanking fields to estimate the torus flux and subtracted it from the flux in the base. Our results were inconclusive, producing aphysical PD $> 100\%$ with large uncertainties. We will note that, in the 5″ polarization map, the PDs of the pixels in the base regions were slightly lower than those of the pixels in the bracketing (background) regions, which suggests that the jet may have a different polarization orientation than the background torus. Higher angular-resolution polarization imaging would be immensely helpful in isolating the jet to test this hypothesis.
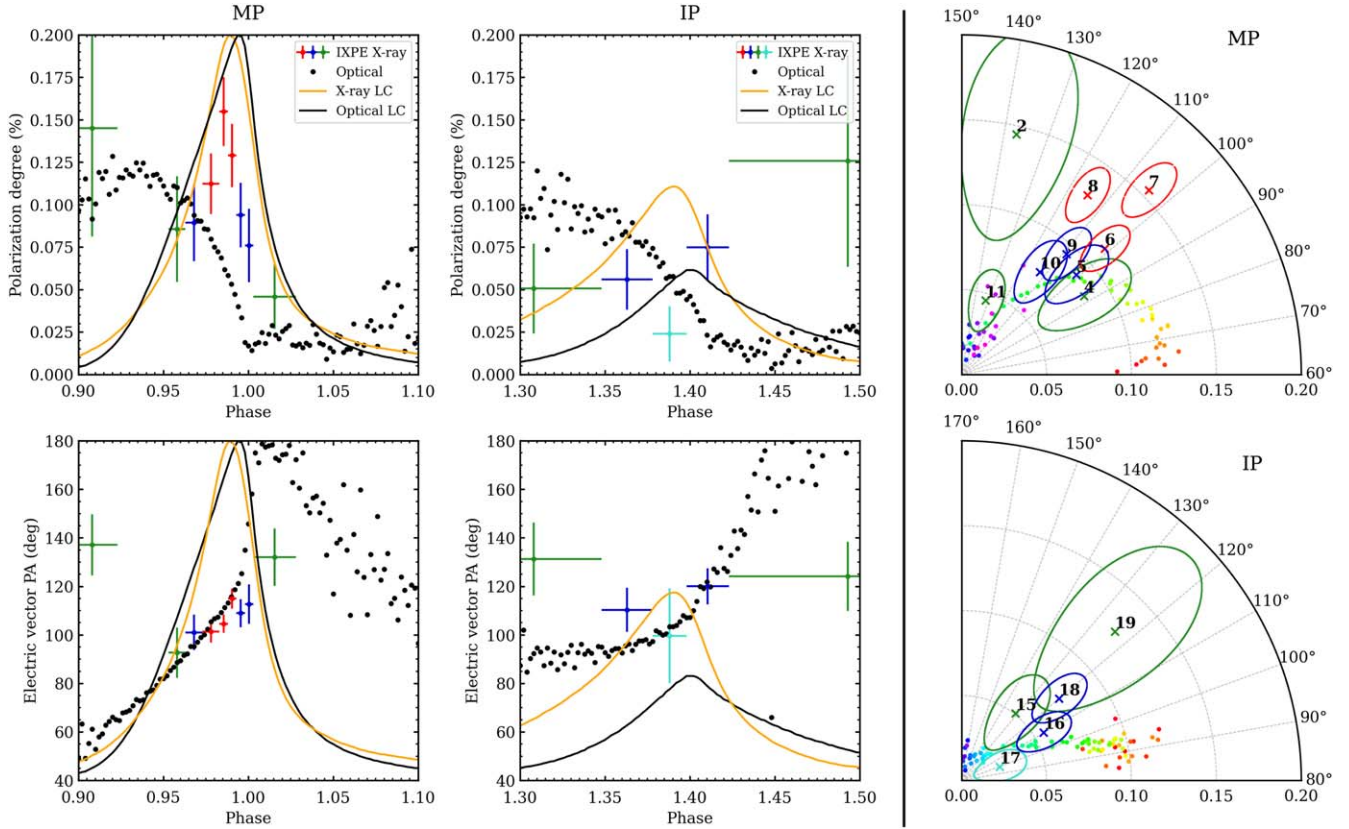
Figure 6. xComparison of X-ray and optical (Słowikowska et al. 2009) PD and PA polarization measurements of the Crab Pulsar. Only MP (ΔP1 = 0.9–1.1) and IP (ΔP2 = 1.3–1.5) are displayed. The red points have $>5\sigma$ significance, the blue $>3\sigma$, and the green $>1.9\sigma$. One turquoise $<1.9\sigma$ bin in the IP is included for continuity. PD and PA vs. phase are shown in the left and middle columns. Normalized light curves for X-ray (orange) and optical (black) are included for reference. Polar representations are shown in the rightmost column, where X-ray measurements with 1σ contours and phase numbering (starting from 1) are plotted against optical values colored from red to blue, to show progression through the pulse. A positive $\sim40°$ X-ray PA sweep can be clearly seen through the MP. See Section 4.2 for a detailed discussion.

4.2. Crab Pulsar

The Crab Pulsar X-ray polarization measurements are plotted against the optical (Słowikowska et al. 2009, obtained via private communication) in traditional PD/PA format (Figure 6), which is useful for model comparison, and in Stokes format (Figure 7). In the traditional plots, polarization parameters below 3σ cannot reliably be reported with 1D error bars, due to PD–PA covariance. Hence, we have restricted the phase range to the MP and the IP and marked marginally significant (and, for continuity, one $<1.9\sigma$ in the IP) measurements with a different color. The polarization values and uncertainties are listed in Table 3.

Among the 20 phase bins, we detect polarization in six phases within the MP and two phases within the IP. In the MP, the PD appears to rise from $\sim7.5\%$ and reach a maximum of $\sim15\%$ near the peak phase, before falling back to its previous level. By comparison, in the optical, the PD is at a constant $\sim12.5\%$ at the rising edge of the pulse and falls to $\sim2.5\%$ right after the optical peak phase. In the X-rays, the PA has an approximately $+40°$ sweep between phases 0.958 and 1.0155. Before the peak, the X-ray PA curve nearly matches the optical PA curve, but afterwards, it appears to rise more slowly and lag behind the optical curve. In the IP, the two significant measurements have PD between 5% and 10%, bracketing one low-significance measurement near the pulse peak. By

comparison, the optical PD is at a constant $\sim10\%$ at the rising edge of the pulse and falls through the pulse to 2.5%. The X-ray IP PA values lie near the optical values and hint at an upward sweep.

Speculating that the low X-ray PD at the center of the IP could be attributed to a rapid angle sweep across this bin, we tried dividing it into two equally spaced bins. However, the polarization still could not be significantly measured in these smaller bins. In addition, we tested for a smooth polarization sweep across this phase range, by partitioning the data in small (0.00017 width) bins, subtracting the background nebula polarization using the simultaneous fit measurements of Section 4.1, and fitting a linear model. The polarization slope was only significant at $\sim1.2\sigma$. With this result, we are not able to conclude whether there is a PA sweep at the IP center.

In Figure 7, we can see that many bins have $>1\sigma$ differences between the optical and X-ray in the Stokes parameters. In the MP, the X-ray Stokes q values fall to a minimum at the center of the pulse, before sweeping rapidly up, while the optical counterpart monotomically increases through the pulse. Both the X-ray and optical Stokes u values dip leading up to the pulse peak, then rise back up, but the X-ray curve has a sharper dip and reaches a lower minimum. In the IP, no conclusive trends can be inferred with only two significant X-ray measurements. Notably, however, the X-ray and optical Stokes values do differ by $\gtrsim1\sigma$ in both IP bins.
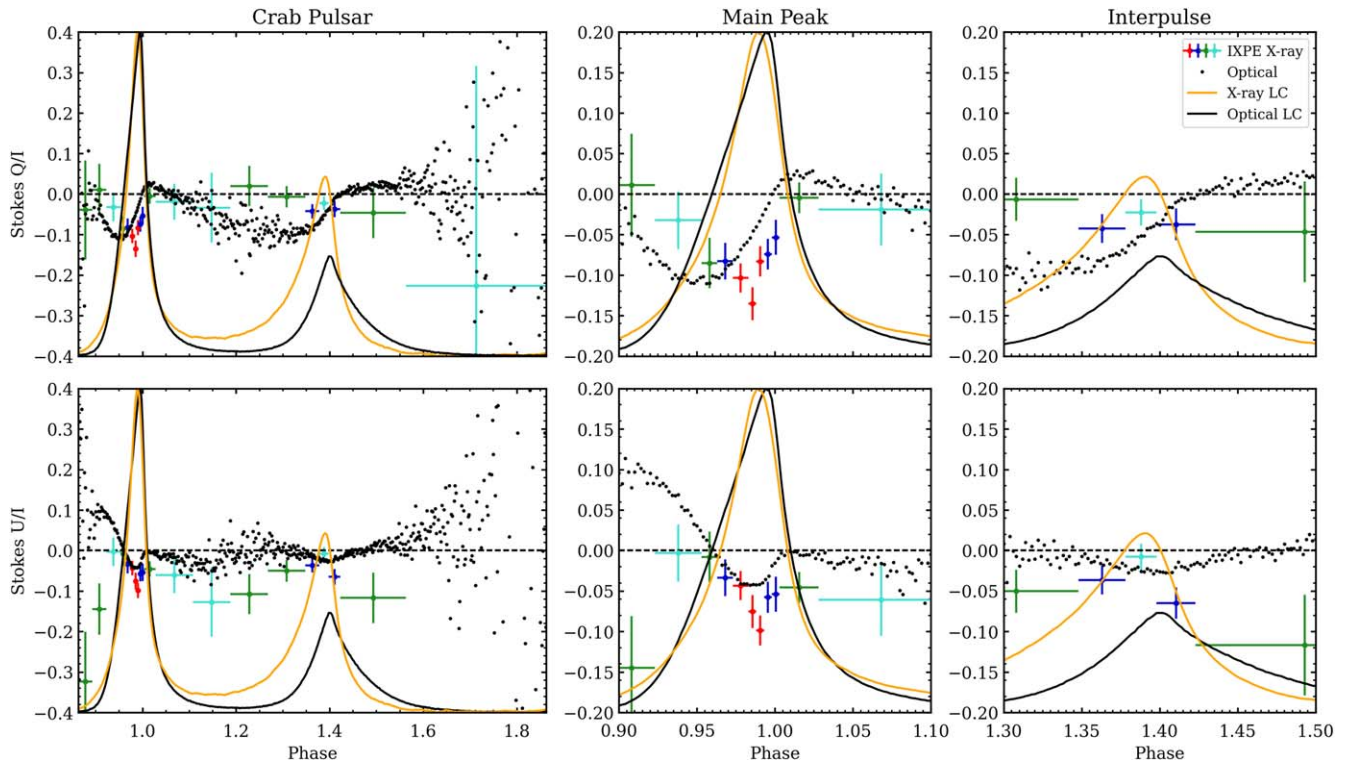
Figure 7. Comparison of X-ray and optical (Słowikowska et al. 2009) Stokes *q* and *u* polarization measurements of the Crab Pulsar. Full phase profile (left), MP (middle, ΔP1 = 0.9–1.1), and IP (right, ΔP2 = 1.3–1.5) are depicted. The red points have >5σ significance, the blue >3σ, the green >1.9σ, and the turquoise <1.9σ. Normalized light curves for X-ray (orange) and optical (black) are included for reference. >1σ differences can be seen between the two energies; see Section 4.2 for a detailed discussion. Different radiation processes or sites may be responsible for the differences in polarization at the two energies.

5. Discussion

While detailed emission models are needed for a full confrontation of these data with theory, we can discuss the qualitative implications of our polarization measurements for the physical conditions in the Crab PWN and pulsar.

From our spectropolarimetric analysis, we find that the PA deviates from that of Region 1 in diametric ways between the north/south and east/west outer regions, as expected in a toroidal geometry. Also, we can see a clear directional dependence of the photon index, suggesting that the energy of the emission is affected not only by synchrotron burnoff, which increases with the distance from the termination shock and was also observed by Weisskopf et al. (2000), but also by some other effect. Although the root cause of this dependence is not clear, it is worth noting that the photon index is hardest in the west, where the PD is smallest, and is softest in south, where the PD is largest. Mori et al. (2004) also report an extended wing of hard emission toward the southwestern edge of the nebula. This observation might be consistent with turbulent (re)acceleration, which would lead to a harder spectrum in a local region of lower polarization. Indeed, Regions 2W and 3W sit adjacent to the western bay, impingement with which could cause increased turbulence.

In the nebula polarization map, the high polarization at the north and south of the torus, with PD ∼ 45%–50%, and the depolarization on the northeast and southwest sides, where the polarization direction changes rapidly, are consistent with the findings of Bucciantini et al. (2023b). In the jet, the PD drops by ∼6% as one moves downstream along the jet and the angle changes relative to the jet axis, from perpendicular to parallel. This observation may be explained by the growth of

kink instabilities along the jet. In the 3D relativistic MHD simulations by Mignone et al. (2013), the jet is subject to instabilities while freely propagating within the PWN flow. Such behavior is seen in CXO monitoring of the Vela pulsar jet (Pavlov et al. 2003). They find that the jet deflection radius increases with the magnetization parameter σ, suggesting that magnetic instabilities are driving the deflection. They also see that the horizontally averaged direction of the magnetic field is initially perpendicular to the flow velocity, but bends and acquires a parallel component at the end. Our jet polarization measurements are consistent with these simulated observations. Alternatively, collision against a dense medium (e.g., an optical filament) may be causing a hoop-stress-confined jet (with an initial field dominated by a toroidal component) to bend, compressing and amplifying the magnetic field parallel to the collision shock front. If accompanied by turbulence, this would also lower the polarization fraction, as seen here.

From our pulsar measurements, we obtain a 3σ upper limit of the bridge (Δ = 1.028–1.348) phase-averaged PD = 22%. The phase-averaged total pulsar polarization is insignificant, with Stokes $q = -0.007 \pm 0.047$ and Stokes $u = -0.075 \pm 0.047$.

Comparing our polarization sweep with that previously measured by Wong et al. (2023) using only the 2022 IXPE Crab observation, a curious difference may be noted: they measured Stokes $u = -0.158 \pm 0.039$ at the single phase bin under the IP peak, which is >2σ higher than the IP Stokes *u* measurements reported here. To investigate this, we ran simultaneous fitting for each observation segment and found that Stokes *u* was approximately −0.15 for the first segment at the single bin under the IP peak (bin 17). Meanwhile, the other segments reported lower values within ±0.05. The large Stokes *u* reported in Wong et al.

(2023) is thus likely a statistical fluctuation and is not changed by the modeling improvements described in the present paper.

We have attempted to compare our pulsar polarization measurements with a simple analytic striped wind model (Del Zanna et al. 2006; Pétri 2013). From our analysis, we find that the pulse morphology is most sensitive to the assumed wind velocity structure, due to the relativistic beaming of emission from the current sheet. If the emission region extends more than a few light cylinder radii (R_{lc}), one finds narrow MP/IP peaks with similar intensity, incompatible with observations. While emission confined within a few R_{lc} produces a plausible intensity profile, the polarization sweeps are quite difficult to reproduce in this simple model. Polarization is more sensitive to the assumed magnetic field geometry, and a simple split monopole model appears to inadequately capture the observed behavior. We note that geometry-dependent reconnection could modulate the emissivity of the current sheet and turbulence growth across the emission zone may affect the PD; these may be important factors to consider in future modeling.

While a detailed treatment goes beyond the scope of this paper, it is important to note that while the excellent optical polarization data of Słowikowska et al. (2009) have been available for some time, no model has been produced that can match its behavior in detail. The fact that IXPE now detects polarization sweep structure at X-ray energies, but with substantial differences with the optical values, provides a new handle on the problem. Since the X-rays are generated by higher-energy electrons, they have different weighting along the emission surface, and possibly different propagation and self-absorption effects, so they provide a new lever to probe this long-standing astrophysical puzzle. Of course, finer and more extended phase-resolved X-ray polarimetry would enhance this probe. In particular, additional IP phase bins are really needed to compare its structure to that seen in the optical. It could also be important to get a few well-measured bins in the bridge region, as this probes emission away from the caustic-dominated peaks. Such data may be attained with very deep IXPE observations or may require a future X-ray polarization mission with better spatial resolution and larger effective area.

ORCID iDs

Josephine Wong ⓘ https://orcid.org/0000-0001-6395-2066
Tsunefumi Mizuno ⓘ https://orcid.org/0000-0001-7263-0296
Niccoló Bucciantini ⓘ https://orcid.org/0000-0002-8848-1392
Roger W. Romani ⓘ https://orcid.org/0000-0001-6711-3286
Yi-Jung Yang ⓘ https://orcid.org/0000-0001-9108-573X
Kuan Liu ⓘ https://orcid.org/0009-0007-8686-9012
Wei Deng ⓘ https://orcid.org/0000-0002-9370-4079
Fei Xie ⓘ https://orcid.org/0000-0002-0105-5826
Maura Pilia ⓘ https://orcid.org/0000-0001-7397-8091
Philip Kaaret ⓘ https://orcid.org/0000-0002-3638-0637
Martin C. Weisskopf ⓘ https://orcid.org/0000-0002-5270-4240
Stefano Silvestri ⓘ https://orcid.org/0000-0002-8665-0105
C.-Y. Ng ⓘ https://orcid.org/0000-0002-5847-2612
Chien-Ting Chen ⓘ https://orcid.org/0000-0002-4945-5079
Iván Agudo ⓘ https://orcid.org/0000-0002-3777-6182
Lucio A. Antonelli ⓘ https://orcid.org/0000-0002-5037-9034
Matteo Bachetti ⓘ https://orcid.org/0000-0002-4576-9337
Luca Baldini ⓘ https://orcid.org/0000-0002-9785-7726
Wayne H. Baumgartner ⓘ https://orcid.org/0000-0002-5106-0463
Ronaldo Bellazzini ⓘ https://orcid.org/0000-0002-2469-7063
Stefano Bianchi ⓘ https://orcid.org/0000-0002-4622-4240
Stephen D. Bongiorno ⓘ https://orcid.org/0000-0002-0901-2097
Raffaella Bonino ⓘ https://orcid.org/0000-0002-4264-1215
Alessandro Brez ⓘ https://orcid.org/0000-0002-9460-1821
Fiamma Capitanio ⓘ https://orcid.org/0000-0002-6384-3027
Simone Castellano ⓘ https://orcid.org/0000-0003-1111-4292
Elisabetta Cavazzuti ⓘ https://orcid.org/0000-0001-7150-9638
Stefano Ciprini ⓘ https://orcid.org/0000-0002-0712-2479
Enrico Costa ⓘ https://orcid.org/0000-0003-4925-8523
Alessandra De Rosa ⓘ https://orcid.org/0000-0001-5668-6863
Ettore Del Monte ⓘ https://orcid.org/0000-0002-3013-6334
Niccoló Di Lalla ⓘ https://orcid.org/0000-0002-7574-1298
Alessandro Di Marco ⓘ https://orcid.org/0000-0003-0331-3259
Immacolata Donnarumma ⓘ https://orcid.org/0000-0002-4700-4549
Victor Doroshenko ⓘ https://orcid.org/0000-0001-8162-1105
Michal Dovčiak ⓘ https://orcid.org/0000-0003-0079-1239
Steven R. Ehlert ⓘ https://orcid.org/0000-0003-4420-2838
Teruaki Enoto ⓘ https://orcid.org/0000-0003-1244-3100
Yuri Evangelista ⓘ https://orcid.org/0000-0001-6096-6710
Sergio Fabiani ⓘ https://orcid.org/0000-0003-1533-0283
Riccardo Ferrazzoli ⓘ https://orcid.org/0000-0003-1074-8605
Javier A. Garcia ⓘ https://orcid.org/0000-0003-3828-2448

Shuichi Gunji ⓘ https://orcid.org/0000-0002-5881-2445
Jeremy Heyl ⓘ https://orcid.org/0000-0001-9739-367X
Wataru Iwakiri ⓘ https://orcid.org/0000-0002-0207-9010
Svetlana G. Jorstad ⓘ https://orcid.org/0000-0001-6158-1708
Vladimir Karas ⓘ https://orcid.org/0000-0002-5760-0459
Fabian Kislat ⓘ https://orcid.org/0000-0001-7477-0380
Jeffery J. Kolodziejczak ⓘ https://orcid.org/0000-0002-0110-6136
Henric Krawczynski ⓘ https://orcid.org/0000-0002-1084-6507
Fabio La Monaca ⓘ https://orcid.org/0000-0001-8916-4156
Luca Latronico ⓘ https://orcid.org/0000-0002-0984-1856
Ioannis Liodakis ⓘ https://orcid.org/0000-0001-9200-4006
Simone Maldera ⓘ https://orcid.org/0000-0002-0698-4421
Alberto Manfreda ⓘ https://orcid.org/0000-0002-0998-4953
Frédéric Marin ⓘ https://orcid.org/0000-0003-4952-0835
Andrea Marinucci ⓘ https://orcid.org/0000-0002-2055-4946
Alan P. Marscher ⓘ https://orcid.org/0000-0001-7396-3332
Herman L. Marshall ⓘ https://orcid.org/0000-0002-6492-1293
Francesco Massaro ⓘ https://orcid.org/0000-0002-1704-9850
Giorgio Matt ⓘ https://orcid.org/0000-0002-2152-0916
Fabio Muleri ⓘ https://orcid.org/0000-0003-3331-3794
Michela Negro ⓘ https://orcid.org/0000-0002-6548-5622
Stephen L. O'Dell ⓘ https://orcid.org/0000-0002-1868-8056
Nicola Omodei ⓘ https://orcid.org/0000-0002-5448-7577
Chiara Oppedisano ⓘ https://orcid.org/0000-0001-6194-4601
Alessandro Papitto ⓘ https://orcid.org/0000-0001-6289-7413
George G. Pavlov ⓘ https://orcid.org/0000-0002-7481-5259
Abel Lawrence Peirson ⓘ https://orcid.org/0000-0001-6292-1911
Matteo Perri ⓘ https://orcid.org/0000-0003-3613-4409
Melissa Pesce-Rollins ⓘ https://orcid.org/0000-0003-1790-8018
Pierre-Olivier Petrucci ⓘ https://orcid.org/0000-0001-6061-3480
Andrea Possenti ⓘ https://orcid.org/0000-0001-5902-3731
Juri Poutanen ⓘ https://orcid.org/0000-0002-0983-0049
Brian D. Ramsey ⓘ https://orcid.org/0000-0003-1548-1524
John Rankin ⓘ https://orcid.org/0000-0002-9774-0560
Ajay Ratheesh ⓘ https://orcid.org/0000-0003-0411-4243
Oliver J. Roberts ⓘ https://orcid.org/0000-0002-7150-9061
Carmelo Sgró ⓘ https://orcid.org/0000-0001-5676-6214
Patrick Slane ⓘ https://orcid.org/0000-0002-6986-6756
Paolo Soffitta ⓘ https://orcid.org/0000-0002-7781-4104
Gloria Spandre ⓘ https://orcid.org/0000-0003-0802-3453
Douglas A. Swartz ⓘ https://orcid.org/0000-0002-2954-4461
Toru Tamagawa ⓘ https://orcid.org/0000-0002-8801-6263
Fabrizio Tavecchio ⓘ https://orcid.org/0000-0003-0256-0995
Roberto Taverna ⓘ https://orcid.org/0000-0002-1768-618X
Allyn F. Tennant ⓘ https://orcid.org/0000-0002-9443-6774

Nicholas E. Thomas ⓘ https://orcid.org/0000-0003-0411-4606
Francesco Tombesi ⓘ https://orcid.org/0000-0002-6562-8654
Alessio Trois ⓘ https://orcid.org/0000-0002-3180-6002
Sergey Tsygankov ⓘ https://orcid.org/0000-0002-9679-0793
Roberto Turolla ⓘ https://orcid.org/0000-0003-3977-8760
Jacco Vink ⓘ https://orcid.org/0000-0002-4708-4219
Kinwah Wu ⓘ https://orcid.org/0000-0002-7568-8765
Silvia Zane ⓘ https://orcid.org/0000-0001-5326-880X

References

Ansoldi, S., Antonelli, L. A., Antoranz, P., et al. 2016, A&A, 585, A133
Baldini, L., Bucciantini, N., Lalla, N. D., et al. 2022, SoftX, 19, 101194
Bucciantini, N., Di Lalla, N., Romani, R. W. R., et al. 2023a, A&A, 672, A66
Bucciantini, N., Ferrazzoli, R., Bachetti, M., et al. 2023b, NatAs, 7, 602
Bühler, R., & Blandford, R. 2014, RPPh, 77, 066901
Chauvin, M., Florén, H. G., Friis, M., et al. 2017, NatSR, 7, 7816
Dean, A. J., Clark, D. J., Stephen, J. B., et al. 2008, Sci, 321, 1183
Del Zanna, L., Volpi, D., Amato, E., & Bucciantini, N. 2006, A&A, 453, 621
Di Marco, A., Soffitta, P., Costa, E., et al. 2023, AJ, 165, 143
Dinsmore, J., & Romani, R. 2024a, LeakageLib, v.1.0.0, Zenodo, doi:10.5281/zenodo.10483298
Dinsmore, J. T., & Romani, R. W. 2024b, ApJ, 962, 183
Dombrovsky, V. A. 1954, DokAN, 94, 1021
Hester, J. J. 2008, ARA&A, 46, 127
Kirk, J. G., Lyubarsky, Y., & Petri, J. 2009, in Neutron Stars and Pulsars (Astrophysics and Space Science Library) Vol. 357 ed. W. Becker (Berlin: Springer), 421
Kislat, F., Clark, B., Beilicke, M., & Krawczynski, H. 2015, APh, 68, 45
Liu, R.-Y., & Wang, X.-Y. 2021, ApJ, 922, 221
Massaro, E., Cusumano, G., Litterio, M., & Mineo, T. 2000, A&A, 361, 695
Mayer, C. H., McCullough, T. P., & Sloanaker, R. M. 1957, ApJ, 126, 468
Mignone, A., Striani, E., Tavani, M., & Ferrari, A. 2013, MNRAS, 436, 1102
Mizuno, T., Ohno, H., Watanabe, E., et al. 2023, PASJ, 75, 1298
Moran, P., Shearer, A., Mignani, R. P., et al. 2013, MNRAS, 433, 2564
Mori, K., Burrows, D. N., Hester, J. J., et al. 2004, ApJ, 609, 186
Ng, C. Y., & Romani, R. W. 2004, ApJ, 601, 479
Novick, R., Weisskopf, M. C., Berthelsdorf, R., Linke, R., & Wolff, R. S. 1972, ApJL, 174, L1
Pavlov, G. G., Teter, M. A., Kargaltsev, O., & Sanwal, D. 2003, ApJ, 591, 1157
Pétri, J. 2013, MNRAS, 434, 2636
Romani, R. 2023, The Shifting Crab Jet 25500050, Chandra Proposal
Shklovsky, I. S. 1953, DoSSR, 90, 983
Slane, P. 2017, in Handbook of Supernovae, ed. A. W. Alsabti & P. Murdin (Berlin: Springer), 2159
Słowikowska, A., Kanbach, G., Kramer, M., & Stefanescu, A. 2009, MNRAS, 397, 103
Trimble, V. 1973, PASP, 85, 579
Vashakidze, M. A. 1954, ACiCh, 147, 11
Weisskopf, M. C., Hester, J. J., Tennant, A. F., et al. 2000, ApJL, 536, L81
Weisskopf, M. C., Silver, E. H., Kestenbaum, H. L., Long, K. S., & Novick, R. 1978, ApJL, 220, L117
Weisskopf, M. C., Soffitta, P., Baldini, L., et al. 2022, JATIS, 8, 026002
Weisskopf, M. C., Tennant, A. F., Yakovlev, D. G., et al. 2011, ApJ, 743, 139
Willingale, R., Aschenbach, B., Griffiths, R. G., et al. 2001, A&A, 365, L212
Wong, J., Romani, R. W., & Dinsmore, J. T. 2023, ApJ, 953, 28
Xie, F., Di Marco, A., La Monaca, F., et al. 2022, Natur, 612, 658
Xie, F., Wong, J., La Monaca, F., et al. 2024, ApJ, 962, 92